Dipole Moments and Transition Dipole Moments Calculated by Pair-Density Functional Theory with State Interaction

Aleksandr O. Lykhin,[1] Moritz K. A. Baumgarten,[2] Donald G. Truhlar,[3*]
and Laura Gagliardi[1,4*]

[1] Department of Chemistry, Pritzker School of Molecular Engineering, The James Franck Institute and Chicago Center for Theoretical Chemistry, The University of Chicago, Chicago, IL 60637, United States

[2] Laboratory of Physical Chemistry, ETH Zurich, 8093 Zurich, Switzerland

[3] Department of Chemistry, Chemical Theory Center, and Minnesota Supercomputing Institute, University of Minnesota, Minneapolis, MN 55455, United States

[4]Argonne National Laboratory, Lemont, Illinois 60439, United States

ABSTRACT. We develop response-function algorithms for dipole moments and transition dipole moments for compressed multistate pair-density functional theory (CMS-PDFT). We use the method of undetermined Lagrange multipliers to derive analytical expressions and validate them using numerical differentiation. We test the accuracy of the magnitudes of predicted ground-state and excited-state dipole moments, the orientations of these dipole moments, and the orientation of transition dipole moments by comparison to experimental data. We show that CMS-PDFT has good accuracy for these quantities, and we also show that – unlike methods that neglect state interaction – CMS-PDFT yields correct behavior for the dipole moment curves in the vicinity of conical intersections. This work, therefore, opens the door to molecular dynamic simulations in strong electric fields, and we envision that CMS-PDFT can now be used to discover chemical reactions that can be controlled by an oriented external electric field upon photoexcitation of the reactants.

1. Introduction

An accurate description of electric dipole moments is crucial for a broad range of applications, including studying chemical reactions controlled by electric fields,[1,2] computing intensities of electronic and vibrational transitions,[3–5] and tuning force fields[6] and machine learning models[7]. The dipole moment of a molecule in a given electronic state is a result of the electron distribution, and – with the physicists' sign convention – it is a vector directed toward the more positive end of the molecule.[8] The transition dipole moment is the vector quantity that determines the strength and polarization of a transition between two electronic states caused by a uniform electric field, such as the electric field of an ultraviolet or visible (UV–vis) electromagnetic wave; its squared magnitude is proportional to the intensity of a transition. The sign of a transition dipole moment is not meaningful on its own because it depends on the arbitrary phases of the wave functions. However, the orientation of a transition dipole moment (aside from the sign of the direction) can be unequivocally defined with respect to the principal axes of inertia to make assignments of bands in spectroscopy.[9]

In the basis of eigenfunctions of the electronic Hamiltonian, the diagonal matrix elements of the electric dipole operator are dipole moments, and the off-diagonal matrix elements are transition dipole moments between different electronic states. Dipole moments calculated as a function of geometry can be used to predict infrared intensities, while transition dipole moments as a function of geometry can be used to predict UV–vis vibronic band intensities.

The dipole moments and transition dipole moments can be calculated by a variety of electronic structure methods, but it can be challenging to obtain high accuracy for strongly correlated electronic states, even for small organic molecules. Strongly correlated states are states where more than one configuration state function is required for a good zero-order wave function; excited electronic states are often strongly correlated, especially if one considers the wide range of geometries needed to describe typical photochemical processes. Therefore, one commonly bases their treatment on reference wave functions obtained by complete-active-space self-consistent-field[10,11] (CASSCF) calculations or state-averaged CASSCF[12] (SA-CASSCF); calculations of this type, with a multiconfigurational reference wave function, are called multireference calculations. One powerful multireference method is the multiconfiguration pair-density functional theory (MC-PDFT), an electronic structure theory that evaluates the electronic energy from the multiconfigurational wave function using the kinetic energy, density, on-top pair density, and an on-top density functional.

Recently, we derived[13] the analytic dipole moment expression for CAS-PDFT, which is MC-PDFT based on a CASSCF reference state. However, that treatment did not yield transition dipole moments.

Here, we use compressed multistate pair-density functional theory (CMS-PDFT),[14] which is a multistate version of MC-PDFT. As in multiconfiguration quasidegenerate perturbation theory,[15] the final step of a CMS-PDFT calculation is diagonalization of a model-space Hamiltonian in the space spanned by the *n* lowest-energy SA-CASSCF eigenvectors. In CMS-PDFT, the model-space Hamiltonian is first formed in an intermediate-state basis consisting of electrostatically compressed states that span the same space as the *n* lowest-energy SA-CASSCF eigenvectors. The CMS-PDFT method predicts the correct topology of crossing states at and near conical intersections, and, more generally, it includes state interaction that becomes important for closely spaced states. CMS-PDFT can be used to calculate both dipole moments and transition dipole moments for strongly correlated states. The accurate prediction of dipole moments at conical intersections becomes critical in molecular dynamics simulations where interaction of the dipole moment with the solvent environment can facilitate population transfer between electronic states.[16] Here we derive and implement the analytical expressions for CMS-PDFT dipole moments and transition dipole moments, and we test their accuracy against the experiment.

For comparison, we also compute dipole moments by state-average pair-density functional theory[17,18] (SA-PDFT) and SA-CASCI and transition dipole moments by SA-CASCI. SA-PDFT also employs SA-CASSCF wave functions but neglects state interaction. Whereas CMS-PDFT obtains all states of interest as orthogonal eigenvectors of the same model-space Hamiltonian by applying the on-top density functional to its diagonal matrix elements in the intermediate-state basis before diagonalization, SA-PDFT computes each state separately by applying the on-top density functional to the corresponding SA-CASSCF eigenvector. On the other hand, SA-CASCI uses the SA-CASSCF wave functions and the conventional energy expressions without density functionals.

The remainder of this paper is organized as follows: Section 2 presents computational details. Section 3 presents the CMS model-space Hamiltonian in a uniform electric field and the equations for the CMS-PDFT dipole moments and transition dipole moments as derivatives of the CMS-PDFT Hamiltonian. Section 4 provides results and discussion. Finally, section 5 has concluding remarks.

2. Computational Details

The analytic dipole moments were coded in the *PySCF*[19,20] package, which was used for all calculations in this article. All calculations in this article use the tPBE on-top functional[21] and the julcc-pVDZ[22] one-electron basis set. In all cases, the model space size in the CMS-PDFT calculations is the same as the number of states averaged in the SA-CASSCF calculations.

3. Theory

3.1 CMS-PDFT Energy in an Electric Field

We consider the usual case where the number *n* of states averaged in SA-CASSCF equals the number of interacting states in the multistate step of CMS-PDFT. The *n* SA-CASSCF eigenvectors are labeled *I*, *J*, …, and we also define two other sets of *n* states that span the same space: intermediate states *P*, *Q*, *R*, *S*, … and CMS eigenvectors *M*, *N*, …. The intermediate states are linear combinations of the SA-CASSCF states

$$|P\rangle = \sum_I |I\rangle\langle I|P\rangle, \tag{1}$$

with the expansion coefficients $\langle I|P\rangle$ chosen to maximize the trace $Q_{a\text{-}a}$ of the classical Coulomb energy of the active electrons:

$$Q_{\text{a-a}} = \frac{1}{2}\sum_P \sum_{ijkl} g_{ijkl} D_{ij}^{PP} D_{kl}^{PP} \ . \tag{2}$$

where *i, j, k*, and *l* are indices of active molecular orbitals, g_{ijkl} is an electron repulsion integral, and D_{ij}^{PP} is an element of the one-electron reduced density matrix for electronic state *P*. In the absence of an external field, the CMS-PDFT energy is evaluated by diagonalizing the effective Hamiltonian matrix in the basis of intermediate states:

$$H^{\text{CMS}}|M\rangle = E_M^{\text{CMS}}|M\rangle, \tag{3}$$

$$\mathbf{H}^{\text{CMS}} = \begin{pmatrix} E_{PP}^{\text{CAS-PDFT}} & \cdots & H_{PQ} \\ \vdots & \ddots & \vdots \\ H_{QP} & \cdots & E_{QQ}^{\text{CAS-PDFT}} \end{pmatrix} \tag{4}$$

where the diagonal elements are CAS-PDFT energies of the intermediate states, and the nondiagonal elements are evaluated as in a conventional configuration interaction (CI) calculation.[14]

A time-independent uniform electric field **F** contributes field-dependent terms representing the interaction of the external electric field with the electrons and the nuclei. The diagonal elements of $\mathbf{H}^{\text{CMS}}$ become

$$\begin{aligned} E_{PP}^{\text{CAS-PDFT}} &= V_{NN} + \sum_{pq} h_{pq} D_{pq}^{PP} + \frac{1}{2}\sum_{pqst} g_{pqst} D_{pq}^{PP} D_{st}^{PP} + E_{\text{OT}}[\rho_P, \Pi_P] \\ &+ \sum_{pq}\sum_{\lambda} F_\lambda \left\{\mathbf{m}_{pq}\right\}_\lambda D_{pq}^{PP} - \sum_{\alpha}\sum_{\lambda} F_\lambda \Omega_\alpha \left\{\mathbf{R}_\alpha\right\}_\lambda \end{aligned} \tag{5}$$

where V_{NN} is the nuclear repulsion, p, q, s, and t are indices of general molecular orbitals, h_{pq} is the one-electron integral, E_{ot} is the on-top density functional of the electron density ρ_P and on-top pair density Π_P of state P, α labels a nucleus, Ω_α is the nuclear charge, $\mathbf{R}_\alpha$ is the coordinate of a nucleus, λ is x, y, or z, $\{\mathbf{v}\}_\lambda$ denotes the λ-component of vector $\mathbf{v}$, F_λ is the electric field strength in direction λ, and $\mathbf{m}_{pq}$ is the integral of the dipole moment vector.

In the presence of the field, the off-diagonal elements of $\mathbf{H}^{\text{CMS}}$ are the elements of a CI Hamiltonian

$$H_{PQ} = \sum_{pq} h_{pq} D_{pq}^{PQ} + \frac{1}{2}\sum_{pqst} g_{pqst} d_{pqst}^{PQ} + \sum_{pq}\sum_{\lambda} F_\lambda \left\{\mathbf{m}_{pq}\right\}_\lambda D_{pq}^{PQ} . \tag{6}$$

where d_{pqst}^{PQ} is an element of the two-electron reduced density matrix.

3.2 CMS-PDFT Dipole Moments

The electric dipole moment equals the first derivative of the energy with respect to the strength of the electric field:[23,24]

$$\mu_\lambda^M = -\left.\frac{dE_M^{CMS}}{dF_\lambda}\right|_{\mathbf{F}=0} . \tag{7}$$

In the basis of CMS-PDFT eigenstates, the CMS-PDFT energy is

$$E_M^{\text{CMS}} = \langle M | \hat{H}^{\text{CMS}} | M \rangle , \tag{8}$$

which can be written in terms of the $\langle M|P\rangle$ expansion coefficients as:

$$E_M^{\text{CMS}} = \sum_{P,Q} \langle M|P\rangle \langle P|\hat{H}^{\text{CMS}}|Q\rangle \langle Q|M\rangle . \tag{9}$$

Next, we differentiate eq (9) and set the electric field strength to zero, as in eq (7). Because the CMS-PDFT energy is stationary with respect to the $\langle M|P\rangle$ expansion coefficients, perturbation of the expansion coefficients with respect to the electric field does not contribute to eq (7), and we obtain

$$\left.\frac{dE_M^{\text{CMS}}}{dF_\lambda}\right|_{\mathbf{F}=0} = \sum_{P,Q} \langle M|P\rangle \left.\frac{dH_{PQ}^{\text{CMS}}}{dF_\lambda}\right|_{\mathbf{F}=0} \langle Q|M\rangle , \tag{10}$$

where H_{PQ}^{CMS} is given in eq (6). This relates the energy derivative to the derivative of the model-space Hamiltonian matrix elements in the intermediate-state basis. These matrix elements, however, are not stationary with respect to the orbital coefficients and CI vectors, and the Hellmann-Feynman theorem does not apply. Instead, we use the Lagrange method of undetermined multipliers to evaluate the derivatives on the right-hand side of eq (10).

We introduce a Lagrangian that is stationary in wave function variables corresponding to nonredundant orbital rotations X_{pq} and unitary transformations of the CI vectors, such as rotations Y_{RA} between a state within and a state outside the model space and rotations Z_{RS} between states within the model space:

$$L_{PQ}^{\mathrm{CMS}} = H_{PQ}^{\mathrm{CMS}} + \sum_{p>q} \frac{\partial E_{\text{SA-CAS}}}{\partial X_{pq}} x_{pq} + \sum_{R,A} \frac{\partial E_{\text{SA-CAS}}}{\partial Y_{RA}} y_{RA} + \sum_{R>S} \frac{\partial Q_{\text{a-a}}}{\partial Z_{RS}} z_{RS}\,, \tag{11}$$

where x_{pq}, y_{RA}, and z_{RS} are Lagrange multipliers associated with the derivatives of state-averaged CASSCF energy $E_{\text{SA-CAS}}$ and classical Coulomb energy $Q_{a\text{-}a}$, and the summations run respectively over orbital indices p and q, over intermediate state indices R and S, and over configuration state functions defined by A. The three sets of Lagrange multipliers are obtained by solving the system of coupled linear equations generated by[25]

$$\frac{\partial L_{PQ}^{\mathrm{CMS}}}{\partial X_{pq}} = \frac{\partial L_{PQ}^{\mathrm{CMS}}}{\partial Y_{RA}} = \frac{\partial L_{PQ}^{\mathrm{CMS}}}{\partial Z_{RS}} = 0\,. \tag{12}$$

The derivatives in eq (10) take the simple form

$$\frac{dH_{PQ}^{\mathrm{CMS}}}{dF_\lambda} = \frac{dL_{PQ}^{\mathrm{CMS}}}{dF_\lambda} = \frac{\partial L_{PQ}^{\mathrm{CMS}}}{\partial F_\lambda}\,. \tag{13}$$

Using the chain rule, we have

$$\frac{\partial L_{PQ}^{\mathrm{CMS}}}{\partial F_\lambda} = \frac{\partial H_{PQ}^{\mathrm{CMS}}}{\partial F_\lambda} + \sum_{p>q} \frac{\partial^2 E_{\text{SA-CAS}}}{\partial F_\lambda \partial X_{pq}} x_{pq} + \sum_{R,A} \frac{\partial^2 E_{\text{SA-CAS}}}{\partial F_\lambda \partial Y_{RA}} y_{RA} + \sum_{R>S} \frac{\partial^2 Q_{\text{a-a}}}{\partial F_\lambda \partial Z_{RS}} z_{RS}\,, \tag{14}$$

where the first term is the Hellmann-Feynman contribution, and the remaining terms are the non-Hellmann-Feynman contributions originating from the nonvariational character of the CMS-PDFT energy.

When $P = Q$, the first term is a derivative of a diagonal element given by eq (5):

$$\begin{aligned} \left.\frac{\partial H_{PQ}^{\text{CMS}}}{\partial F_{\lambda}}\right|_{P=Q} &= \frac{\partial}{\partial F_{\lambda}}\left\{\sum_{pq} h_{pq} D_{pq}^{PP} + \frac{1}{2}\sum_{pqst} g_{pqst} D_{pq}^{PP} D_{st}^{PP} + E_{\text{ot}}^{PP}\right. \\ &\left. + \sum_{pq}\sum_{\eta} F_{\eta}\left\{\mathbf{m}_{pq}\right\}_{\eta} D_{pq}^{PP} - \sum_{\alpha}\sum_{\eta} F_{\eta}\Omega_{\alpha}\left\{\mathbf{R}_{\alpha}\right\}_{\eta}\right\} \quad . \\ &= \sum_{pq}\left\{\mathbf{m}_{pq}\right\}_{\lambda} D_{pq}^{PP} - \sum_{A}\Omega_{\alpha}\left\{\mathbf{R}_{\alpha}\right\}_{\lambda} \end{aligned} \tag{15}$$

When $P \neq Q$, this derivative takes a different form that follows from eqs (5) and (6):

$$\begin{aligned} \left.\frac{\partial H_{PQ}^{\text{CMS}}}{\partial F_{\lambda}}\right|_{P\neq Q} &= \frac{\partial}{\partial F_{\lambda}}\left\{\sum_{pq} h_{pq} D_{pq}^{PQ} + \frac{1}{2}\sum_{pqst} g_{pqst} d_{pqst}^{PQ} + \right. \\ &\left. + \sum_{pq}\sum_{\eta} F_{\eta}\left\{\mathbf{m}_{pq}\right\}_{\eta} D_{pq}^{PQ}\right\} = \sum_{pq}\left\{\mathbf{m}_{pq}\right\}_{\lambda} D_{pq}^{PQ} \end{aligned} \tag{16}$$

By nesting outcomes of eqs (15) and (16) into eq (10), we obtain the nuclear part of the dipole moment and the electronic Hellmann-Feynman contribution

$$\begin{aligned} &\sum_{P,Q}\langle M|P\rangle \frac{\partial H_{PQ}^{\text{CMS}}}{\partial F_{\lambda}}\langle Q|M\rangle = \\ &\sum_{P,Q}\langle M|P\rangle \sum_{pq}\left\{\mathbf{m}_{pq}\right\}_{\lambda} D_{pq}^{PQ}\langle Q|M\rangle \\ &-\sum_{\alpha}\Omega_{\alpha}\left\{\mathbf{R}_{\alpha}\right\}_{\lambda}\sum_{P}\langle M|P\rangle\langle P|M\rangle = \\ &\sum_{P,Q}\langle M|P\rangle \sum_{pq}\left\{\mathbf{m}_{pq}\right\}_{\lambda} D_{pq}^{PQ}\langle Q|M\rangle - \sum_{\alpha}\Omega_{\alpha}\left\{\mathbf{R}_{\alpha}\right\}_{\lambda} \end{aligned} \tag{17}$$

The second and third terms in eq (11) are reminiscent of those in SA-PDFT and CMS-PDFT analytical gradients[25,26] but involve electric dipole integrals instead of nuclear derivatives of one-electron integrals, in particular:

$$\sum_{p>q}\frac{\partial^{2} E_{\text{SA-CAS}}}{\partial F_{\lambda}\partial X_{pq}} x_{pq}^{M} = \sum_{pq}\left\{\mathbf{m}_{pq}\right\}_{\lambda}\sum_{J}\omega_{J}\sum_{s}\left(x_{ps}^{M} D_{sq}^{J} - x_{sq}^{M} D_{ps}^{J}\right), \tag{18}$$

$$\sum_{R,A}\frac{\partial^{2} E_{\text{SA-CAS}}}{\partial F_{\lambda}\partial Y_{RA}} y_{RA}^{M} = \sum_{pq}\left\{\mathbf{m}_{pq}\right\}_{\lambda}\sum_{J,\Lambda}\omega_{J} y_{J\Lambda}^{M}\left[\left\langle J\middle|\hat{E}_{pq}\middle|\Lambda\right\rangle + \left\langle \Lambda\middle|\hat{E}_{pq}\middle|J\right\rangle\right]. \tag{19}$$

Here, M is the index of the adiabatic CMS-PDFT state for which the dipole moment is computed, E_{pq} is the one-electron excitation operator,[27] J runs over reference SA-CASSCF states with weights ω, and Λ runs over configuration state functions. Finally, the last term in eq (11) is zero by construction because $Q_{\text{a-a}}$ does not depend on the electric field.

Next, we compare dipole moment expressions in CMS-PDFT, SA-PDFT, and single-state MC-PDFT. These methods apply the on-top density functional respectively to the compressed-state intermediate states, the SA-CASSCF eigenvectors, and the state-specific CASSCF eigenvectors. The nuclear component of the electric dipole moment for classically treated nuclei is

$$\xi_0 = \sum_{\alpha} \Omega_{\alpha} \left\{ \mathbf{R}_{\alpha} \right\}_{\lambda} . \tag{20}$$

The electric dipole moment for the given state M in CMS-PDFT is

$$\left\{ \mu_{\lambda}^{M} \right\}^{\text{CMS-PDFT}} = \xi_0 - \sum_{P,Q} \langle M | P \rangle (\xi_1 + \xi_2 + \xi_3) \langle Q | M \rangle , \tag{21}$$

$$\xi_1 = \sum_{pq} \left\{ \mathbf{m}_{pq} \right\}_{\lambda} D_{pq}^{PQ} , \tag{22}$$

$$\xi_2 = \sum_{pq} \left\{ \mathbf{m}_{pq} \right\}_{\lambda} \sum_{J} \omega_J \sum_{s} (x_{ps}^{M} D_{sq}^{J} - x_{sq}^{M} D_{ps}^{J}) , \tag{23}$$

$$\xi_3 = \sum_{pq} \left\{ \mathbf{m}_{pq} \right\}_{\lambda} \sum_{J,\Lambda} \omega_J y_{J\Lambda}^{M} \left[\left\langle J \middle| \hat{E}_{pq} \middle| \Lambda \right\rangle + \left\langle \Lambda \middle| \hat{E}_{pq} \middle| J \right\rangle \right] , \tag{24}$$

the electric dipole moment for the given state I in SA-PDFT is

$$\left\{ \mu_{\lambda}^{I} \right\}^{\text{SA-PDFT}} = \xi_0 - (\xi_1 + \xi_2 + \xi_3) , \tag{25}$$

$$\xi_1 = \sum_{pq} \left\{ \mathbf{m}_{pq} \right\}_{\lambda} D_{pq}^{I} , \tag{26}$$

$$\xi_2 = \sum_{pq} \left\{ \mathbf{m}_{pq} \right\}_{\lambda} \sum_{J} \omega_J \sum_{s} (x_{ps}^{I} D_{sq}^{J} - x_{sq}^{I} D_{ps}^{J}) , \tag{27}$$

$$\xi_3 = \sum_{pq} \left\{ \mathbf{m}_{pq} \right\}_{\lambda} \sum_{J,\Lambda} \omega_J y_{J\Lambda} \left[\left\langle J \middle| \hat{E}_{pq} \middle| \Lambda \right\rangle + \left\langle \Lambda \middle| \hat{E}_{pq} \middle| J \right\rangle \right] , \tag{28}$$

and the electric dipole moment for the ground state in SS-PDFT is

$$\left\{ \mu_{\lambda} \right\}^{\text{SS-PDFT}} = \xi_0 - (\xi_1 + \xi_2 + \xi_3) , \tag{29}$$

$$\xi_1 = \sum_{pq} \left\{ \mathbf{m}_{pq} \right\}_{\lambda} D_{pq} , \tag{30}$$

$$\xi_2 = \sum_{pq} \left\{ \mathbf{m}_{pq} \right\}_{\lambda} \sum_{s} (x_{ps} D_{sq} - x_{sq} D_{ps}) , \tag{31}$$

$$\xi_3 = \sum_{pq} \left\{ \mathbf{m}_{pq} \right\}_{\lambda} \sum_{J} y_J \left[\left\langle J \middle| \hat{E}_{pq} \middle| 0 \right\rangle + \left\langle 0 \middle| \hat{E}_{pq} \middle| J \right\rangle \right] . \tag{32}$$

The SA-CASSCF eigenvectors, the CMS-PDFT intermediate states, and the CMS-PDFT eigenvectors all span the same space, and when they overlap, eq (21) reduces to

$$\left\{\mu_\lambda^M\right\}^{\text{CMS-PDFT}} = \xi_0 - \sum_{P,Q} \delta_{MP}(\xi_1 + \xi_2 + \xi_3)\delta_{QM} \ . \tag{33}$$

When $P \neq Q$, the sum is precisely zero because of the two Kronecker deltas. When $P = Q$, only a single term with $P = M$ survives the summation yielding eqs (26)-(28) of the SA-PDFT method for ξ_1, ξ_2, and ξ_3, respectively. Thus, the CMS-PDFT expression reduces to SA-PDFT one when there is no interaction between intermediate states, and the classical Coulomb energies are already maximized in the space of state-averaged references. Also, note that eq (27) can be written in terms of state-averaged density matrices, as was shown in previous work:[26]

$$\xi_2 = \sum_{pq} \left\{\mathbf{m}_{pq}\right\}_\lambda \sum_s (x_{ps} D_{sq}^{SA} - x_{sq} D_{ps}^{SA}) \,. \tag{34}$$

3.3 CMS-PDFT Transition Dipole Moments

The CMS-PDFT Hamiltonian can be expanded in a Taylor series in the presence of an external electric field as

$$\hat{H}^{\text{CMS}}(\mathbf{F}) = \hat{H}_0^{\text{CMS}} - \hat{\boldsymbol{\mu}} \cdot \mathbf{F} - \ldots, \tag{35}$$

where $\hat{H}_0^{\text{CMS}}$ is the field-independent CMS-PDFT Hamiltonian and $\hat{\boldsymbol{\mu}}$ is the dipole operator. By truncating this expansion at the linear term, the off-diagonal Hamiltonian matrix elements become

$$H^{MN}(\mathbf{F}) = \left\langle M(\mathbf{F}) \middle| \hat{H}_0^{\text{CMS}} - \hat{\boldsymbol{\mu}} \cdot \mathbf{F} \middle| N(\mathbf{F}) \right\rangle . \tag{36}$$

Because the H^{MN} elements are zero by construction, their derivative with respect to the electric field component F_λ is also zero:

$$\left.\frac{dH^{MN}(\mathbf{F})}{dF_\lambda}\right|_{\mathbf{F}=0} = -\left\langle M \middle| \hat{\mu}_\lambda \middle| N \right\rangle + \left\langle \frac{\partial M(\mathbf{F})}{\partial F_\lambda} \middle| \hat{H}_0^{\text{CMS}} \middle| N \right\rangle + \left\langle M \middle| \hat{H}_0^{\text{CMS}} \middle| \frac{\partial N(\mathbf{F})}{\partial F_\lambda} \right\rangle = 0 \,. \tag{37}$$

The first term on the right-hand side is a transition dipole moment, and it can be written as

$$\begin{aligned} \mu_\lambda^{MN} &= \left\langle M \middle| \hat{\mu}_\lambda \middle| N \right\rangle \\ &= \left\langle \frac{\partial M(\mathbf{F})}{\partial F_\lambda} \middle| \hat{H}_0^{\text{CMS}} \middle| N \right\rangle + \left\langle M \middle| \hat{H}_0^{\text{CMS}} \middle| \frac{\partial N(\mathbf{F})}{\partial F_\lambda} \right\rangle . \end{aligned} \tag{38}$$

On the other hand, direct differentiation of the off-diagonal elements leads to

$$H^{MN}(\mathbf{F}) = \left\langle M(\mathbf{F}) \middle| \hat{H}^{CMS}(\mathbf{F}) \middle| N(\mathbf{F}) \right\rangle, \tag{39}$$

$$\left.\frac{dH^{MN}(\mathbf{F})}{dF_\lambda}\right|_{\mathbf{F}=0} = \langle M | \left.\frac{d\hat{H}^{\text{CMS}}(\mathbf{F})}{dF_\lambda}\right|_{\mathbf{F}=0} | N \rangle + \left\langle \frac{\partial M(\mathbf{F})}{\partial F_\lambda} \middle| \hat{H}_0^{\text{CMS}} \middle| N \right\rangle + \left\langle M \middle| \hat{H}_0^{\text{CMS}} \middle| \frac{\partial N(\mathbf{F})}{\partial F_\lambda} \right\rangle = 0\,. \tag{40}$$

Combining eqs (38) and (40), the transition dipole moment in CMS-PDFT takes the form

$$\mu_\lambda^{MN} = -\langle M | \left.\frac{d\hat{H}^{\text{CMS}}(\mathbf{F})}{dF_\lambda}\right|_{\mathbf{F}=0} | N \rangle\,. \tag{41}$$

Using a completeness relation, this derivative is transformed into

$$\begin{aligned} \left\{\mu_\lambda^{MN}\right\}^{CMS} &= -\sum_{P,Q} \langle M | P \rangle \left.\frac{dH_{PQ}^{\text{CMS}}(\mathbf{F})}{dF_\lambda}\right|_{\mathbf{F}=0} \langle Q | N \rangle \\ &= -\sum_{P,Q} \langle M | P \rangle (\xi_1 + \xi_2 + \xi_3) \langle Q | N \rangle \end{aligned}, \tag{42}$$

which is analogous to the CMS-PDFT dipole moment, except that state |*N*> is in place of state |*M*>, while ξ_1, ξ_2, and ξ_3 are identical to the terms used in dipole moment as given by eqs (30)-(32). Note that the nuclear contribution to the transition dipole moment is zero because of the orthogonality of the CMS-PDFT states.

4. Results and Discussion

4.1 Comparison of Numerical and Analytic Dipole Moments

First, we tested our implementation of analytical CMS-PDFT dipole moments and transition dipole moments by carrying out the derivative of eq (7) by converged finite differences. We did this for water, furan, and furan cation using the two-point central difference formulas where diagonal and off-diagonal elements of the Hamiltonians include the field terms. The finite difference expression of the dipole moment of electronic state *M* is

$$\left\{\mu_\lambda^{M}\right\}^{\text{CMS-PDFT}} = \frac{E_M(-F_\lambda) - E_M(+F_\lambda)}{2F_\lambda}\,, \tag{43}$$

And the finite difference expression used to calculate the transition dipole moment connecting electronic states *M* and *N* is

$$\left\{\mu_\lambda^{MN}\right\}^{\text{CMS-PDFT}} = \sum_{P,Q} \langle M | P \rangle \frac{H_{PQ}(-F_\lambda) - H_{PQ}(+F_\lambda)}{2F_\lambda} \langle Q | M \rangle\,. \tag{44}$$

We set the energy convergence threshold to 10^{-11} hartree (see the Supporting Information). We found that the numerical derivatives agreed with the analytical expressions within 10^{-3} D; this confirms the correctness of the analytic expressions and their coding.

4.2 Dipole Moments in Regions of Strong Interaction of Electronic States

Phenol. We calculated the dipole moments of phenol as a function of the O-H bond distance. The SA-CASSCF wave function was averaged over the lowest three singlet electronic states, which are strongly coupled along this coordinate. The (12e,11o) active space included three π-orbitals and three π*-orbitals of the aromatic ring, the lone pair orbital, and two pairs of σ and σ* orbitals primarily localized on the C-O and O-H bonds. The orbitals are shown in Figure S2; figures and tables with the prefix S are in supporting Information. This choice of active orbitals allowed a continuous change of the active space at the longer O-H distances. We scanned the potential energy curves and dipole moment curves as we decreased the O-H bond distance from 3.0 to 0.9 Å and kept the remaining nuclear degrees of freedom frozen at their ground-state equilibrium values; the results for CMS-PDFT are in Figure 1.

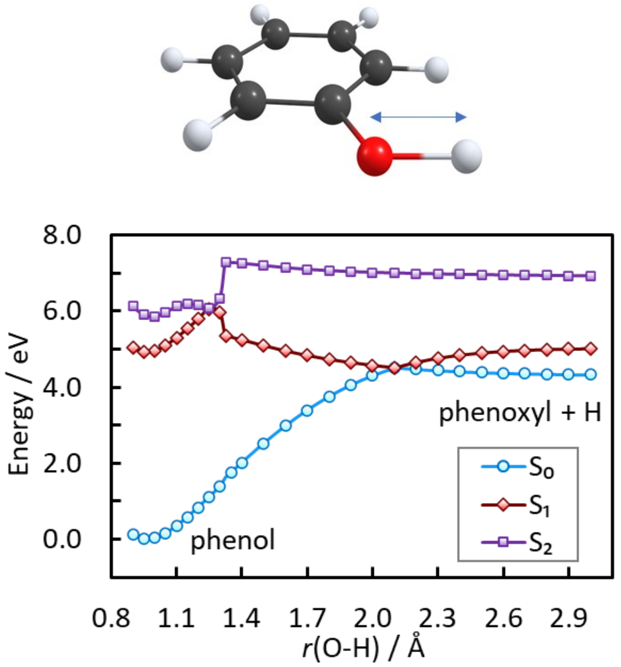

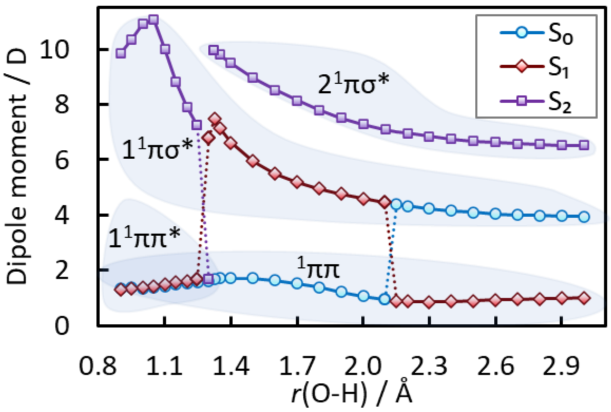

Figure 1. Top: Phenol. Middle: Unrelaxed scan of CMS-PDFT adiabatic potential energy curves along the r(O-H) coordinate in phenol. Bottom: Dipole moment curves for the same scan.

In the Franck-Condon region, the $S_1(\pi\pi^*)$ and $S_2(\pi\sigma^*)$ states are well separated from the ground state, with excitation energies of 4.93 and 5.83 eV, respectively. The ground-state bond dissociation energy is calculated to be 4.33 eV, which is in good agreement with the experimental value[28] of 4.18 eV. The second dissociation channel requires the energy of 5.03 eV, while the third one is much higher and is located at 6.93 eV above the ground-state minimum. A moderate gap between the two lowest dissociation channels leads to the relaxation of the bright S_1 state through two competitive dissociation paths producing a ground or excited phenoxyl radical and hydrogen atom, as was discussed previously.[28]

Upon elongating the O-H bond from the equilibrium distance [r(O-H) = 0.965 Å], the S_1 and S_2 excited states approach one another at ~1.3 Å, swapping their diabatic characters. The system reaches a second avoided crossing at ~2.2 Å, at which the S_0 state acquires a repulsive $\pi\sigma^*$ character. The changing character of the states has a strong effect on the dipole moments. In most geometries, the predicted dipole moment curves are smooth functions of O-H coordinate with a slight discontinuity at ~1.3 Å caused by the close-lying third excited singlet. The bottom panel of Figure 1 shows a physically reasonable change in dipole moments when the system passes through the near-degeneracy regions. Because the electronic states have very different dipole moments, an electric field will change their relative energies together with the geometries and energies of the conical intersections.

Figure 2 compares the CMS-PDFT results to the SA-PDFT ones. The CMS-PDFT potential energy curves shown in Figure 2 (top, left) are similar to those of the SA-PDFT method except for the regions where states approach one another. The lack of state interaction in SA-PDFT leads to unphysical double crossings (Figure 2, bottom), with the location of ππ /πσ* character switching being shifted toward shorter O-H bonds (Figure 2, top, right).

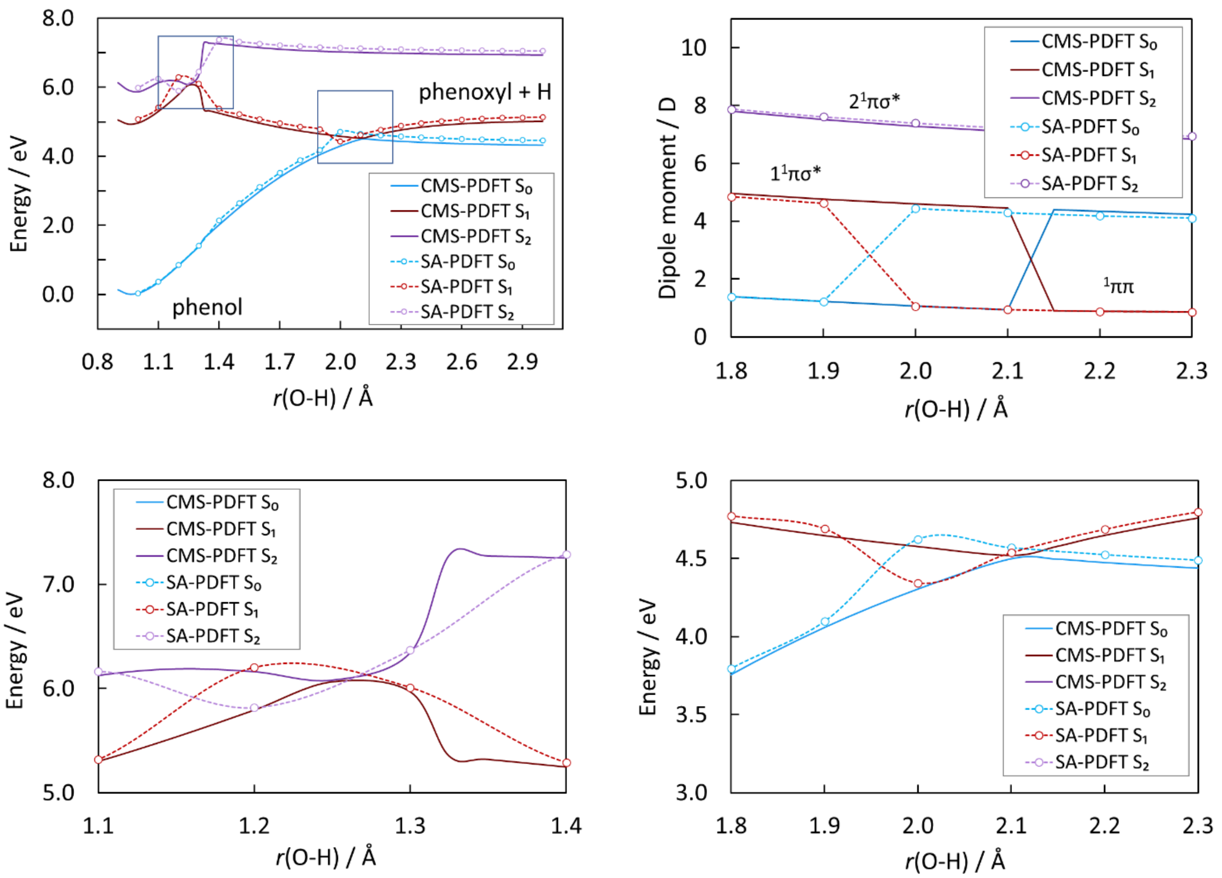

Figure 2. Potential energy (top left panel) and dipole moment (top right panel) curves for phenol as calculated by CMS-PDFT and SA-PDFT. The panels in the bottom line are zoomed in on the areas outlined by rectangles in the upper left panel.

Spiro Cation. Next, we consider the crossing states in 2,2′,6,6′-tetrahydro-4H,4′H-5,5′-spirobi[cyclopenta-[c]pyrrole], which is called the spiro cation and is illustrated in Figure 3. The spiro cation is a challenging mixed-valence system.[29] In the most symmetrical D_{2d} configuration, the unpaired electron is delocalized over the left and right pyrrole subunits, which are twisted with respect to each other by 90°. The high symmetry leads to a zero-dipole moment at the D_{2d} configuration. However, this structure is unstable in the S_0 ground state due to a pseudo-Jahn-Teller distortion. Consequently, the spiro cation tends to distort into either of the two C_{2v} minima, where the unpaired electron is mostly localized on the left or right.[14]

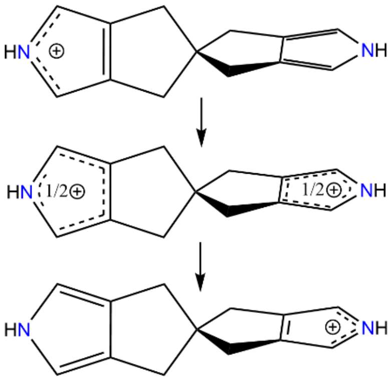

Figure 3. Spiro cation structure with a hole being localized on either side (top and bottom) or delocalized (middle).

The energy and dipole moment along a unitless reaction coordinate connecting two localized structures through the D_{2d} structure (at 0) is illustrated in Figure 4. In an earlier study,[14] it was shown that potential energy curves predicted by CMS-PDFT agree well with CASPT2 predictions. Here, we investigate the problem using CMS-PDFT and SA-PDFT methods employing the same (11e,10o) active space that spans the π-systems of pyrrole rings, as shown in Figure S3. As expected, the dipole moments at the two C_{2v} geometries are equal in magnitude but opposite in direction.

We performed SA-CASSCF, SA-PDFT, and CMS-PDFT calculations in which the SA-CASSCF reference wave function is based on 11 active electrons in 10 active orbitals (11e,10o), and the energy is averaged over the two lowest singlet states of A_2 symmetry. The active orbitals are shown in Figure S3. Figure 4 (top) shows that SA-PDFT qualitatively fails to reproduce the avoided crossing and gives unphysical dips in the potential energy curves (as found in the previous work) and unphysical dipole moment curves for both electronic states near the conical intersection, Figures 4 (bottom) and S3. This illustrates how the independent calculations of the two SA-PDFT energies make the treatment of close-lying states very inaccurate. Employing a model-space diagonalization in an appropriate intermediate basis as the final step, CMS-PDFT eliminates the unphysical behavior at the symmetrical geometry and gives physically reasonable continuous dipole moment curves as well as a physical energy curve. We conclude that CMS-PDFT is more reliable than SA-PDFT for calculating dipole moments of strongly correlated systems where the interaction between states becomes important.

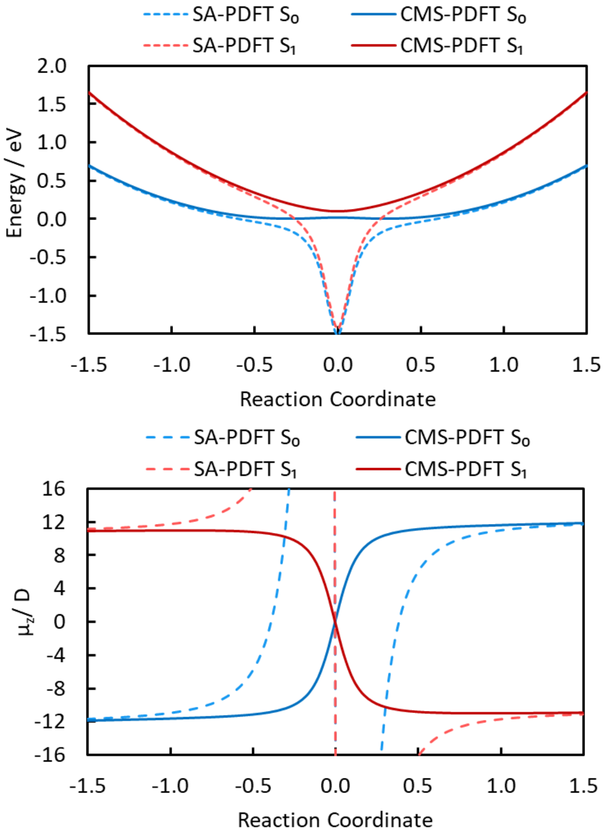

Figure 4. Potential energy curves[14] (top) and projection of the dipole moment on the principal axis (bottom) of the spiro cation as functions of the unitless breathing reaction coordinate (see ref 14 for a mathematical definition of the reaction coordinate). Reprinted partially with permission from ref. 14. Copyright 2020 American Chemical Society.

4.3 Tests on a Dataset of 20 Aromatic Molecules

To assess the accuracy of CMS-PDFT for dipole moments, we analyzed a dataset of 20 aromatic molecules (Figure 5) for which the experimental dipole moments are available for the ground and the lowest excited states; all excited states in the dataset are singlet $S_1(\pi\pi^*)$ states. The S_1 states have greater multireference character than the S_0 states. We use a principal-axes-of-inertia coordinate frame in which the moments of inertia are in the order $I_a < I_b < I_c$. All molecules in the dataset possess a symmetry plane that makes the *c*-component of the dipole moment and transition dipole moment precisely zero. Our later discussion also involves the *a*-axis of this coordinate frame. The dipole moments of the ground states are for the ground-state equilibrium geometries, and those for the excited states are for the excited-state equilibrium geometries. When computing the S_1 dipole moments, we chose the lowest S_1 minimum if multiple minima were located. When calculating transition dipole moments, we used the S_0 equilibrium geometry.

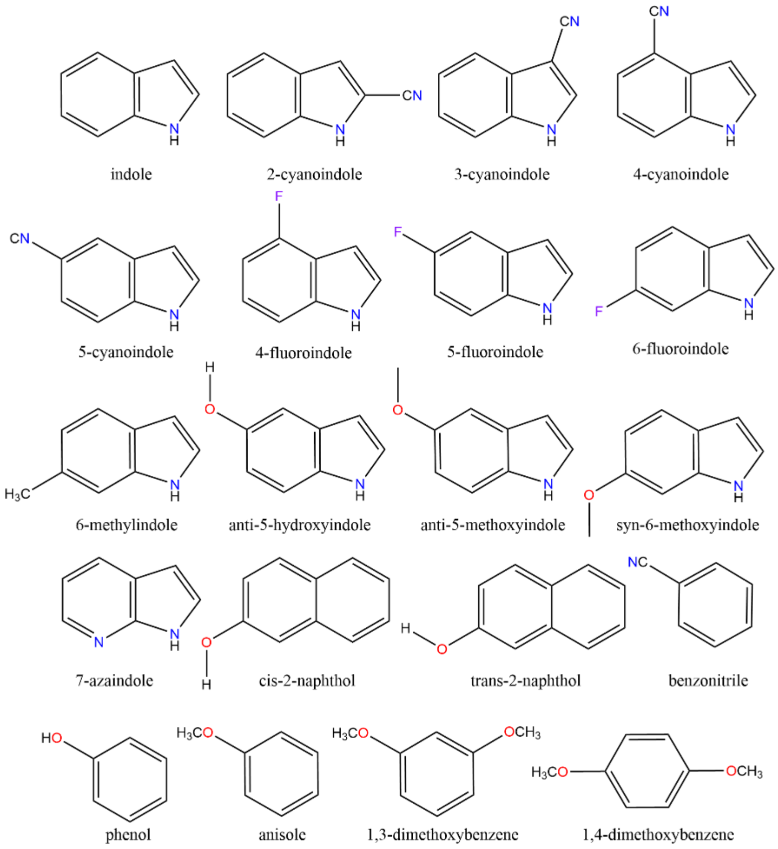

Figure 5. Structures of investigated molecules.

The active spaces included the π systems of the aromatic rings and the lone pairs of heteroatoms, except that we did not include the lone pairs of fluorine atoms in the active spaces because of their low energies. Additionally, in the case of cyanoindoles, in addition to the π- and π*-orbitals of the conjugated rings, we also included a second pair of π and π*-orbitals of the nitrile group orthogonal to the π-system of the fused rings.

The reference SA-CASSCF wave functions were averaged over the two lowest-energy singlet states. The dipole moments were computed using CMS-PDFT and SA-PDFT at the geometries optimized by the corresponding methods. We also used the complete active space configuration interaction method[30,31] (SA-CASCI) to obtain dipole moments at the CMS-PDFT optimized geometries; the SA-CASSCF orbitals were employed in the SA-CASCI calculations. The dipole moments were evaluated by energy differentiation in the CMS-PDFT (eq (21)) and SA-PDFT (eq (25)) calculations and as the expectation value of the dipole moment operator in the case of SA-CASCI calculations. Note that SA-CASCI wave functions based on SA-CASSCF are not variationally stable for individual electronic states, and SA-CASCI values correspond to unrelaxed densities.

The experimental dipole moments were derived from the 0-0 bands. All calculated dipole moments are for optimized geometries and are not averaged over vibrational motions. This is reasonable in most cases since a typical vibrational averaging of the dipole moments is expected to be small.[32] For some conformationally flexible molecules, however, this may be an issue of concern. For example, the dipole moment of 7-azaindole promoted to the S_1 origin at ~34630 cm^{-1} is 2.30(3) D.[33] However, in the excitation +280 cm^{-1} above the S_1 origin, it is 4.6(1) D.[34] Such difference can be attributed to the intramolecular proton transfer from the pyrrole nitrogen to the pyridine nitrogen triggered by excitation of the N-H vibrational mode. As a check, Table S1 shows that the CMS-PDFT and SA-CASCI adiabatic $S_1 \leftarrow S_0$ excitation energies are close to the experimentally measured energies of the 0-0 bands.

Magnitudes of the Dipole Moments. When computing dipole moments, we used analytic formulas obtained by energy differentiation in the case of CMS-PDFT and SA-PDFT. For the SA-CASCI method, we used expectation values (response than response theory) with unrelaxed densities for electronic states. Therefore, S_0 and S_1 dipole moments are based on unrelaxed densities.

The absolute magnitudes of the experimental and computed dipole moments are summarized in Table 1. The dipole moments range in size from 1.01 to 8.92 D. The relative errors in the magnitude of equilibrium dipole moments with respect to gas-phase experimental values are shown in Figures 6 and 7. In the ground state, the mean absolute percentage error (MAPE) of the CMS-PDFT, SA-CASCI, and SA-PDFT methods are quite similar: 10%, 8%, and 9%, respectively. However, in the excited S_1 state, the SA-CASCI error is almost doubled, with a MAPE of 16%, whereas the MAPEs of the CMS-PDFT and SA-PDFT calculations are still small, respectively 10% and 9%. This indicates the importance of including a larger amount of the correlation energy.

Table 1. Calculated and experimental S_0 and S_1 dipole moments (D).

No.	Compound	Active space	Experiment.		CMS-PDFT		SA-CASCI		SA-PDFT	
			S_0	S_1	S_0	S_1	S_0	S_1	S_0	S_1
1	indole[35,36]	(10e,9o)	1.96(1)	1.86(1)	2.38	2.08	1.88	1.51	2.36	2.17
2	2-cyanoindole[37]	(14e,13o)	3.71(1)	5.21(1)	4.04	4.85	3.65	4.39	3.75	6.05
3	3-cyanoindole[38]	(14e,13o)	5.90(1)	5.35(1)	6.23	5.71	5.77	5.23	6.23	5.72
4	4-cyanoindole[39]	(14e,13o)	6.31(1)	8.92(1)	6.99	7.19	6.14	6.02	6.81	8.32
5	5-cyanoindole[36]	(14e,13o)	7.14(4)	8.17(3)	7.74	7.64	6.66	6.33	7.55	8.28
6	4-fluoroindole[40]	(10e,9o)	3.41(4)	2.99(4)	3.73	3.24	3.62	3.16	3.71	3.28
7	5-fluoroindole[36,40]	(10e,9o)	3.62(1)	3.32(2)	4.00	3.64	3.87	3.48	4.04	3.69
8	6-fluoroindole[40]	(10e,9o)	2.51(3)	3.38(3)	3.24	3.32	3.01	3.02	3.18	3.60
9	6-methylindole[41]	(10e,9o)	1.84(1)	1.74(1)	2.25	2.00	1.81	1.46	2.24	2.09
10	anti-5-hydroxyindole[36,42]	(12e,10o)	2.15(2)	1.54(3)	2.10	1.92	2.27	2.00	2.36	1.61
11	anti-5-methoxyindole[43,44]	(12e,10o)	1.59(3)	1.14(6)	1.47	1.32	1.66	1.44	1.81	1.07
12	syn-6-methoxyindole[43,45]	(12e,10o)	2.89(3)	3.46(2)	3.23	3.37	2.95	2.92	3.14	3.79
13	7-azaindole[33]	(10e,9o)	1.59(3)	2.30(3)	1.81	2.02	1.43	1.55	1.76	2.31
14	cis-2-naphthol[46]	(12e,11o)	1.01(1)	1.17(1)	1.02	1.13	1.23	1.34	1.00	1.26
15	trans-2-naphthol[47]	(12e,11o)	1.36(1)	1.44(1)	1.56	1.55	1.58	1.51	1.50	1.68
16	benzonitrile[48]	(10e,10o)	4.48(1)	4.57(1)	4.62	4.62	4.43	4.37	4.64	4.77
17	phenol[49,50]	(8e,7o)	1.224(8)	1.30	1.28	1.33	1.44	1.47	1.27	1.38
18	anisole[51]	(8e,7o)	1.26	2.19(4)	1.41	1.60	1.33	1.47	1.29	1.92
19	1,3-dimethoxybenzene[51]	(10e,8o)	1.19(5)	1.42(8)	1.32	1.49	1.32	1.46	1.27	1.62
20	1,4-dimethoxybenzene[51]	(10e,8o)	2.23(1)	2.76(1)	2.24	2.67	2.53	2.85	2.18	2.84
	mean absolute percentage error				10.4	9.6	8.0	15.5	9.1	9.0

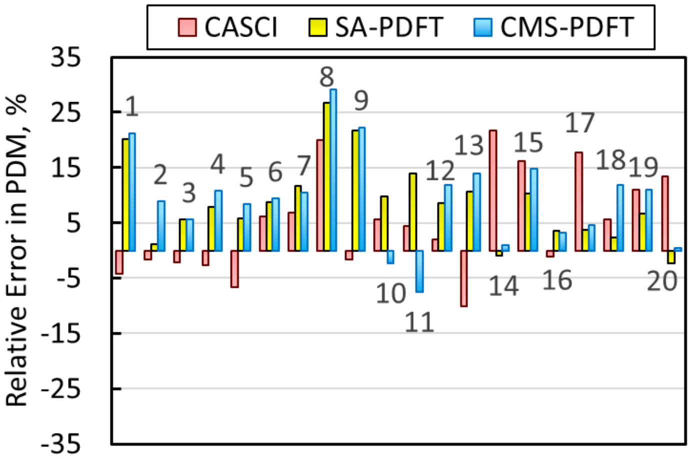

Figure 6. Relative errors (vs. experiment) in the dipole moments (PDMs) of the S_0 state. The labels correspond to the structures in Figure 5 and Table 1.

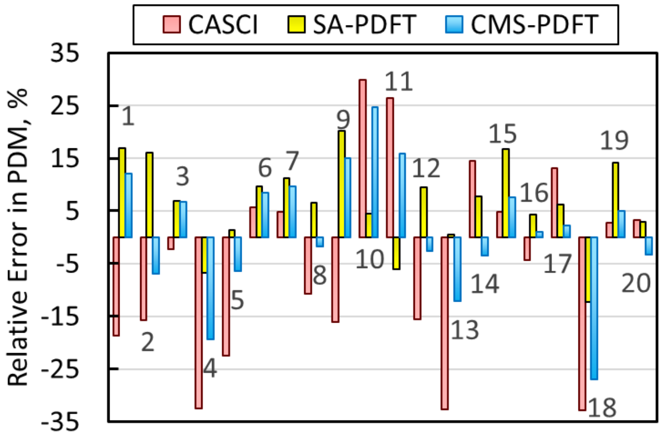

Figure 7. Relative errors (vs. experiment) in the dipole moments (PDMs) of the S_1 state. The labels correspond to the structures in Figure 5 and Table 1.

Orientations of Dipole Moments and Transition Dipole Moments. When computing transition dipole moments, we used the analytic formula for CMS-PDFT. For SA-CASCI, we computed transition dipole moments as $<0|\mathbf{m}|1>$ with unrelaxed densities.

The orientations of the dipole moments were characterized by the angles θ that they make with the main inertial axis (a-axis) in a given electronic state; because the excited-state optimized geometry is different from the ground-state one, the principal axes are slightly rotated. In the case of $S_1 \leftarrow S_0$ transition dipole moments, θ was defined with respect to the a-axis in the ground-state frame. A positive sign of θ implies a clockwise rotation of the main inertial a-axis onto the dipole moment vector, as illustrated in Figure 8.

The angles of the dipole moments are given in Table 2, and the errors as compared to the experiment are reported in Figure 9. Note that some of the entries in Figure 9 are omitted as the experimental orientation of dipole moments and transition dipole moments are either unavailable or trivial due to the high symmetry. Therefore, such data points were eliminated from averaging when calculating mean absolute percentage errors.

For the dipole moments, the mean absolute percentage errors of CMS-PDFT values of θ are 8% for both S_0 and S_1. The SA-CASCI predictions are close to that value, with $\theta(S_0)$ equal to 6% and sufficiently greater for $\theta(S_1)$ of 13%. There is no significant improvement in CMS-PDFT calculations over SA-CASCI results for the orientation of the transition dipole.

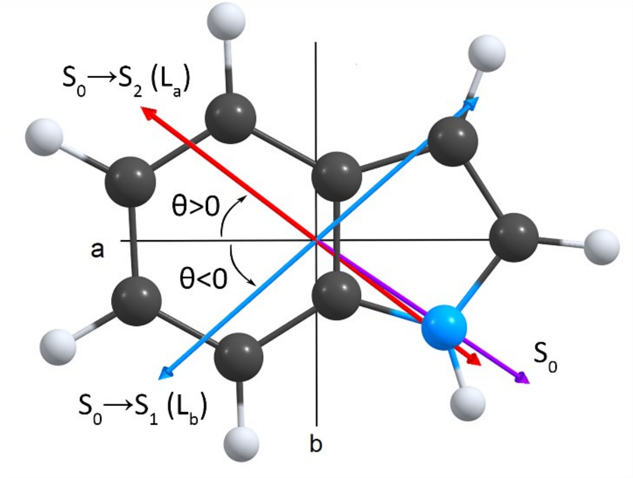

Figure 8. Orientation of dipole moment and transition dipole moment in indole. The lengths of arrows are arbitrary.

Table 2. Experimental 0-0 gaps E_{00} (eV), computed adiabatic excitation energies E_{ad} (eV), and angles (deg) of the dipole moments and transition dipole moments with the principal inertia *a*-axis.[a]

		Experiment			CMS-PDFT			SA-CASCI		
		Θ (S_0)	Θ (S_1)	θ ($S_1 \leftarrow S_0$)	Θ (S_0)	Θ (S_1)	θ ($S_1 \leftarrow S_0$)	Θ (S_0)	Θ (S_1)	θ ($S_1 \leftarrow S_0$)
1	indole[35,36]	±45.5(4)	±33.0(6)	±38.3(2)	44.0	37.1	-23.9	48.6	41.9	-48.4
2	2-cyanoindole[37]	±15.7	±7.8	±45.9(2)	16.7	7.7	73.7	14.8	6.4	42.2
3	3-cyanoindole[38]	±45.3	±39.3	±15.3(1)	47.2	44.7	-20.1	45.6	42.3	10.1
4	4-cyanoindole[39]	±15.5	±1.86	±30.7(1)	13.6	9.4	-44.4	17.8	14.0	-70.2
5	5-cyanoindole[36]	±13(2)	±11(2)	±3(3)	14.8	13.0	10.5	16.3	14.1	-36.6
6	4-fluoroindole[40]	±40(1)	±37(1)	±63.1(1)	34.1	32.1	-78.6	42.1	41.3	78.1
7	5-fluoroindole[36,40]	±26(1)	±19(1)	±59.0(1)	26.1	20.4	-48.0	26.2	21.6	-64.0
8	6-fluoroindole[40]	±10(4)	±12(3)	±23.5(1)	27.1	22.6	10.7	19.6	13.9	-10.6
9	6-methylindole[41]	±79.4(1)	±83.7	±21(2)	65.9	58.2	0.0	69.0	62.5	-26.1
10	anti-5-hydroxyindole[36,42]	±5(5)	±6(6)	±54	-7.1	11.5	46.0	0.0	14.2	60.9
11	anti-5-methoxyindole[43,44]	±15(1)	±69(1)	±58.4(1)	0.0	-36.1	-54.0	-9.4	-38.2	-70.8
12	syn-6-methoxyindole[43,45]	±86(1)	±83(1)	±36.2(1)	86.2	80.5	29.7	80.9	77.3	17.0
13	7-azaindole[33]	±24(2)	±14(2)	±14.2	-15.6	-17.8	-9.7	-29.4	-33.7	-24.6
14	cis-2-naphthol[46]	±70.1(4)	±97.8(4)	N/A	88.1	89.4	-57.2	-56.6	-58.7	-68.3
15	trans-2-naphthol[47]	±73.7	±44.5	N/A	-60.6	-54.1	-66.8	-84.1	-78.4	-77.6
16	benzonitrile[48]	0	0	90	0.0	0.0	90.0	0.0	0.0	90.0
17	phenol[49,50]	±83.8	±77.1	N/A	-83.3	-80.6	84.1	74.4	77.8	84.8
18	anisole[51]	±56.7	±43.4	±69.70(1)	45.9	44.6	85.0	68.8	64.7	84.3
19	1,3-dimethoxybenzene[51]	±15(3)	±29(5)	±14.5(1)	-41.2	-38.5	-7.8	-20.0	-20.2	-7.7
20	1,4-dimethoxybenzene[51]	90	90	90	90.0	90.0	90.0	90.0	90.0	90.0
	MAE				7.7	7.7	12.9	5.8	12.6	13.1

[a] A positive sign of the angles *θ* refers to a clockwise rotation of the inertial *a*-axis onto the dipole moment or transition dipole moment vector.

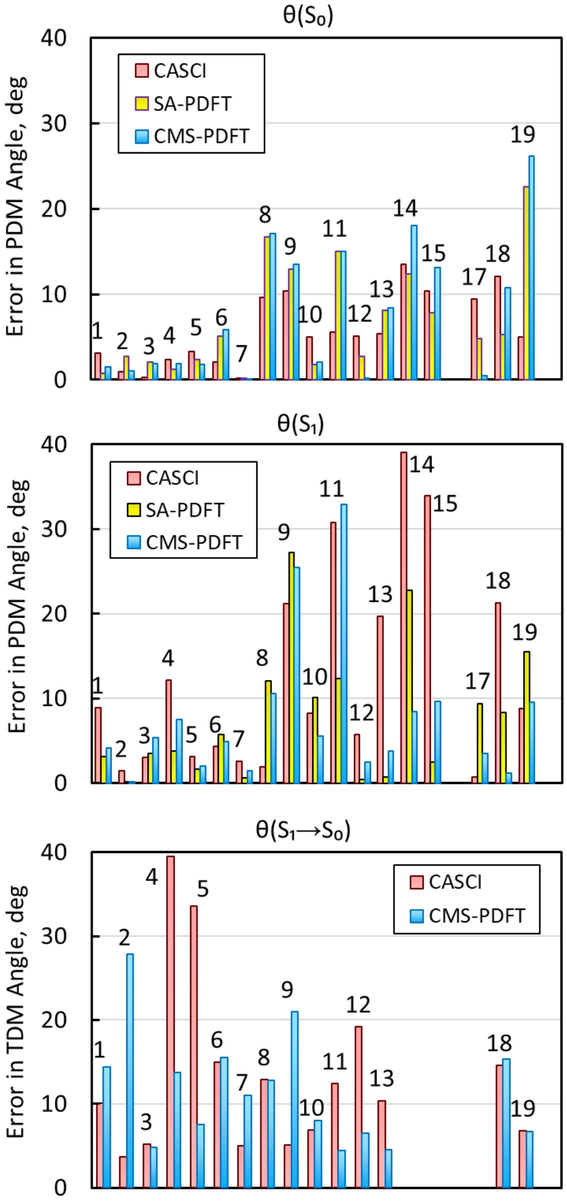

Figure 9. Absolute errors in the orientation of dipole moments of S_0 (top) and S_1 (middle) states and the $S_1 \leftarrow S_0$ transition dipole moments (bottom) compared to experimental references. The labels correspond to the structures in Figure 5. The data points are omitted if experimental references are not available or the orientation of the dipole moment is trivial due to symmetry.

5. Concluding Remarks

We have developed and implemented CMS-PDFT analytic dipole moments and transition dipole moments. The method is currently available in the pyscf-forge collection of extensions of the *PySCF* package (https://github.com/pyscf/pyscf-forge).

We showed that by using CMS-PDFT with an SA-CASSCF reference wave function and translated on-top density functional, one can compute the magnitude of equilibrium dipole moments for the ground and excited electronic states with a relative error of about 10% from the experiment. A similar error has been found with the SA-PDFT method. However, when electronic states are strongly coupled, for instance, near a conical intersection, CMS-PDFT outperforms SA-PDFT, which often fails to provide even qualitatively correct dipole moment curves. The error in the orientation of CMS-PDFT dipole moments is about 8% for both ground and excited states. The alternative SA-CASCI method shows a similar error for the S_0 state of 6% but deteriorates for the strongly correlated state S_1 with an error of 13%.

We envision that dipole moments computed by CMS-PDFT can be used in several ways: (i) to discover photochemical reactions that can be controlled by an oriented external electric field; (ii) to make assignments of excited electronic states based on the orientation of the transition dipole moments; (iii) to compute oscillator strengths of the electronic transitions in molecular dynamics simulations or for assigning spectra; (iv) to generate properties of the multireference excited states that can be used as the training data for machine learning.

Item (i) from this list is an interesting frontier area because the interaction of a molecular dipole moment with an external electric field can facilitate chemical transformations or slow them down. The theoretical prediction of accurate dipole moments using computational tools can be important for identifying *optimal* oriented electric fields[52] for electrostatic field control. Such reactions have already been studied in molecular junctions[53] but are currently limited to single-molecule experiments; however, the development of large-area molecular junctions[54,55] offers promise for industrial-scale electrostatic catalysis.

The current limitation of CMS-PDFT is the size of the active space chosen for the underlying SA-CASSCF calculations and the potential degeneracy of the CMS intermediate states, which can be troublesome for CMS-PDFT in some cases.

Supporting Information

The Supporting Information is available free of charge at https://pubs.acs.org/doi/10.1021/acs.jpca.3c01142.

> Comparison of numerical and analytical dipole moments, natural orbitals of the (12e,11o) active space in phenol, natural orbitals of the (11e,10o) active space of spiro cation, the dipole moment of spiro cation with (11e,10o) active space, experimental 0-0 gaps and computed adiabatic excitation energies (PDF)

Acknowledgment

The authors are grateful to Jie Bao and Matt Hermes for continuing discussions of analytic gradients and the CMS-PDFT method. The present work is supported in part by the National Science Foundation under grant CHE-2054723 and in part by the Air Force Office Scientific Research by Grant FA9550-20-1-0360. In addition, we thank the Research Computing Center at the University of Chicago and the Minnesota Supercomputing Institute at the University of Minnesota for computational resources.

Author Information

Corresponding Authors

Donald G. Truhlar - Department of Chemistry, Chemical Theory Center, and Minnesota Supercomputing Institute, University of Minnesota, 207 Pleasant Street SE, Minneapolis, Minnesota 55455, United States
orcid.org/0000-0002-7742-7294
Email: truhlar@umn.edu

Laura Gagliardi - Department of Chemistry, Pritzker School of Molecular Engineering, The James Franck Institute and Chicago Center for Theoretical Chemistry, The University of Chicago, Chicago, IL 60637, United States; Argonne National Laboratory, Lemont, Illinois 60439, United States
orcid.org/0000-0001-5227-1396
Email: lgagliardi@uchicago.edu

Authors

Aleksandr O. Lykhin - Department of Chemistry, Pritzker School of Molecular Engineering, The James Franck Institute and Chicago Center for Theoretical Chemistry, The University of Chicago, Chicago, IL 60637, United States
orcid.org/0000-0002-9366-5866

Moritz K. A. Baumgarten - Laboratory of Physical Chemistry, ETH Zurich, 8093 Zurich, Switzerland
orcid.org/0000-0002-5214-2655

Complete contact information is available at: https://pubs.acs.org/10.1021/acs.jpca.3c01142

Notes

The authors declare no competing financial interest.

References

(1) Aragonès, A. C.; Haworth, N. L.; Darwish, N.; Ciampi, S.; Bloomfield, N. J.; Wallace, G. G.; Diez-Perez, I.; Coote, M. L. Electrostatic Catalysis of a Diels-Alder Reaction. *Nature* **2016**, *531*, 88–91.

(2) Huang, X.; Tang, C.; Li, J.; Chen, L.-C.; Zheng, J.; Zhang, P.; Le, J.; Li, R.; Li, X.; Liu, J. et al. Electric Field–Induced Selective Catalysis of Single-Molecule Reaction. *Sci. Adv.* **2019**, *5*, eaaw3072.

(3) Gastegger, M.; Behler, J.; Marquetand, P. Machine Learning Molecular Dynamics for the Simulation of Infrared Spectra. *Chem. Sci.* **2017**, *8*, 6924–6935.

(4) Neugebauer, J.; Reiher, M.; Kind, C.; Hess, B. A. Quantum Chemical Calculation of Vibrational Spectra of Large Molecules - Raman and IR Spectra for Buckminsterfullerene. *J. Comput. Chem.* **2002**, *23*, 895–910.

(5) Lodi, L.; Tennyson, J.; Polyansky, O. L. A Global, High Accuracy Ab Initio Dipole Moment Surface for the Electronic Ground State of the Water Molecule. *J. Chem. Phys.* **2011**, *135*, 034113.

(6) Nebgen, B.; Lubbers, N.; Smith, J. S.; Sifain, A. E.; Lokhov, A.; Isayev, O.; Roitberg, A. E.; Barros, K.; Tretiak, S. Transferable Dynamic Molecular Charge Assignment Using Deep

Neural Networks. *J. Chem. Theory Comput.* **2018**, *14*, 4687–4698.

(7) Pereira, F.; Aires-de-Sousa, J. Machine Learning for the Prediction of Molecular Dipole Moments Obtained by Density Functional Theory. *J. Cheminform.* **2018**, *10*, 43.

(8) Hovick, J. W.; Poler, J. C. Misconceptions in Sign Conventions: Flipping the Electric Dipole Moment. *J. Chem. Educ.* **2005**, *82*, 889.

(9) Yong, H.; Zotev, N.; Stankus, B.; Ruddock, J. M.; Bellshaw, D.; Boutet, S.; Lane, T. J.; Liang, M.; Carbajo, S.; Robinson, J. S. et al. Determining Orientations of Optical Transition Dipole Moments Using Ultrafast X-Ray Scattering. *J. Phys. Chem. Lett.* **2018**, *9*, 6556–6562.

(10) Siegbahn, P.; Heiberg, A.; Roos, B.; Levy, B. A Comparison of the Super-CI and the Newton-Raphson Scheme in the Complete Active Space SCF Method. *Phys. Scr.* **1980**, *21*, 323–327.

(11) Siegbahn, P. E. M.; Almlöf, J.; Heiberg, A.; Roos, B. O. The Complete Active Space SCF (CASSCF) Method in a Newton-Raphson Formulation with Application to the HNO Molecule. *J. Chem. Phys.* **1981**, *74*, 2384–2396.

(12) Werner, H. J.; Meyer, W. A Quadratically Convergent MCSCF Method for the Simultaneous Optimization of Several States. *J. Chem. Phys.* **1981**, *74*, 5794–5801.

(13) Lykhin, A. O.; Truhlar, D. G.; Gagliardi, L. Dipole Moment Calculations Using Multiconfiguration Pair-Density Functional Theory and Hybrid Multiconfiguration Pair-Density Functional Theory. *J. Chem. Theory Comput.* **2021**, *17*, 7586–7601.

(14) Bao, J. J.; Zhou, C.; Truhlar, D. G. Compressed-State Multistate Pair-Density Functional Theory. *J. Chem. Theory Comput.* **2020**, *16*, 7444–7452.

(15) Nakano, H. Quasidegenerate Perturbation Theory with Multiconfigurational Self-Consistent-Field Reference Functions. *J. Chem. Phys.* **1993**, *99*, 7983.

(16) Huix-Rotllant, M.; Schwinn, K.; Pomogaev, V.; Farmani, M.; Ferré, N.; Lee, S.; Choi, C. H. Photochemistry of Thymine in Solution and DNA Revealed by an Electrostatic Embedding QM/MM Combined with Mixed-Reference Spin-Flip TDDFT. *J. Chem. Theory Comput.* **2023**, *19*, 147–156.

(17) Sharma, P.; Bernales, V.; Truhlar, D. G.; Gagliardi, L. Valence ππ∗ Excitations in Benzene Studied by Multiconfiguration Pair-Density Functional Theory. *J. Phys. Chem. Lett.* **2019**, *10*, 75–81.

(18) Calio, P. B.; Truhlar, D. G.; Gagliardi, L. Nonadiabatic Molecular Dynamics by Multiconfiguration Pair-Density Functional Theory. *J. Chem. Theory Comput.* **2022**, *18*, 614–

622.

(19) Sun, Q.; Berkelbach, T. C.; Blunt, N. S.; Booth, G. H.; Guo, S.; Li, Z.; Liu, J.; McClain, J. D.; Sayfutyarova, E. R.; Sharma, S. et al. PySCF: The Python-based Simulations of Chemistry Framework. *WIREs Comput. Mol. Sci.* **2018**, *8*, e1340.

(20) Sun, Q.; Zhang, X.; Banerjee, S.; Bao, P.; Barbry, M.; Blunt, N. S.; Bogdanov, N. A.; Booth, G. H.; Chen, J.; Cui, Z.-H. et al. Recent Developments in the PySCF Program Package. *J. Chem. Phys.* **2020**, *153*, 024109.

(21) Manni, G. L.; Carlson, R. K.; Luo, S.; Ma, D.; Olsen, J.; Truhlar, D. G.; Gagliardi, L. Multiconfiguration Pair-Density Functional Theory. *J. Chem. Theory Comput.* **2014**, *10*, 3669–3680.

(22) Papajak, E.; Truhlar, D. G. Convergent Partially Augmented Basis Sets for Post-Hartree−Fock Calculations of Molecular Properties and Reaction Barrier Heights. *J. Chem. Theory Comput.* **2011**, *7*, 10–18.

(23) Jensen, F. *Introduction to Computational Chemistry*, Third Edit.; John Wiley & Sons, Ltd: Chichester, UK, 2017.

(24) Kraka, E.; Gauss, J.; Cremer, D. Determination and Use of Response Densities. *J. Mol. Struct. THEOCHEM* **1991**, *234*, 95–126.

(25) Bao, J. J.; Hermes, M. R.; Scott, T. R.; Sand, A. M.; Lindh, R.; Gagliardi, L.; Truhlar, D. G. Analytic Gradients for Compressed Multistate Pair-Density Functional Theory. *Mol. Phys.* **2022**, *120*, e2110534.

(26) Scott, T. R.; Hermes, M. R.; Sand, A. M.; Oakley, M. S.; Truhlar, D. G.; Gagliardi, L. Analytic Gradients for State-Averaged Multiconfiguration Pair-Density Functional Theory. *J. Chem. Phys.* **2020**, *153*, 014106.

(27) Helgaker, T.; Jørgensen, P.; Olsen, J. *Molecular Electronic-Structure Theory*; Wiley: Chichester, 2000.

(28) Xu, X.; Yang, K. R.; Truhlar, D. G. Diabatic Molecular Orbitals, Potential Energies, and Potential Energy Surface Couplings by the 4-Fold Way for Photodissociation of Phenol. *J. Chem. Theory Comput.* **2013**, *9*, 3612–3625.

(29) Dong, S. S.; Huang, K. B.; Gagliardi, L.; Truhlar, D. G. State-Interaction Pair-Density Functional Theory Can Accurately Describe a Spiro Mixed Valence Compound. *J. Phys. Chem. A* **2019**, *123*, 2100–2106.

(30) Knowles, P. J.; Handy, N. C. A New Determinant-Based Full Configuration Interaction

Method. *Chem. Phys. Lett.* **1984**, *111*, 315–321.

(31) Olsen, J.; Roos, B. O.; Jørgensen, P.; Jensen, H. J. A. Determinant Based Configuration Interaction Algorithms for Complete and Restricted Configuration Interaction Spaces. *J. Chem. Phys.* **1988**, *89*, 2185–2192.

(32) Paulson, L. O.; Kaminský, J.; Anderson, D. T.; Bouř, P.; Kubelka, J. Theoretical Study of Vibrationally Averaged Dipole Moments for the Ground and Excited C═O Stretching States of Trans-Formic Acid. *J. Chem. Theory Comput.* **2010**, *6*, 817–827.

(33) Kang, C.; Yi, J. T.; Pratt, D. W. Stark Effects in the Gas Phase: Dipole Moment of 7-Azaindole in Its Ground and Electronically Excited States. *Chem. Phys. Lett.* **2006**, *423*, 7–12.

(34) Young, J. W.; Pozun, Z. D.; Jordan, K. D.; Pratt, D. W. Excited Electronic State Mixing in 7-Azaindole. Quantitative Measurements Using the Stark Effect. *J. Phys. Chem. B* **2013**, *117*, 15695–15700.

(35) Kang, C.; Korter, T. M.; Pratt, D. W. Experimental Measurement of the Induced Dipole Moment of an Isolated Molecule in Its Ground and Electronically Excited States: Indole and Indole–H_2O. *J. Chem. Phys.* **2005**, *122*, 174301.

(36) Wilke, J.; Wilke, M.; Brand, C.; Meerts, W. L.; Schmitt, M. On the Additivity of Molecular Fragment Dipole Moments of 5-Substituted Indole Derivatives. *ChemPhysChem* **2016**, *17*, 2736–2743.

(37) Hebestreit, M.-L.; Lartian, H.; Henrichs, C.; Kühnemuth, R.; Meerts, W. L.; Schmitt, M. Excited State Dipole Moments and Lifetimes of 2-Cyanoindole from Rotationally Resolved Electronic Stark Spectroscopy. *Phys. Chem. Chem. Phys.* **2021**, *23*, 10196–10204.

(38) Schneider, M.; Hebestreit, M.-L.; Lindic, M. M.; Parsian, H.; Torres-Boy, A. Y.; Álvarez-Valtierra, L.; Meerts, W. L.; Kühnemuth, R.; Schmitt, M. Rotationally Resolved Electronic Spectroscopy of 3-Cyanoindole and the 3-Cyanoindole–Water Complex. *Phys. Chem. Chem. Phys.* **2018**, *20*, 23441–23452.

(39) Hebestreit, M. L.; Schneider, M.; Lartian, H.; Betz, V.; Heinrich, M.; Lindic, M.; Choi, M. Y.; Schmitt, M. Structures, Dipole Moments and Excited State Lifetime of Isolated 4-Cyanoindole in Its Ground and Lowest Electronically Excited Singlet States. *Phys. Chem. Chem. Phys.* **2019**, *21*, 14766–14774.

(40) Wilke, J.; Wilke, M.; Brand, C.; Spiegel, J. D.; Marian, C. M.; Schmitt, M. Modulation of the L_a/L_b Mixing in an Indole Derivative: A Position-Dependent Study Using 4-, 5-, and 6-

Fluoroindole. *J. Phys. Chem. A* **2017**, *121*, 1597–1606.

(41) Hebestreit, M. L.; Böschen, H.; Lartian, H.; Meerts, W. L.; Schmitt, M. Rotationally Resolved Electronic Spectroscopy of 6-Methylindole: Structures, Transition Moments, and Permanent Dipole Moments of Ground and Excited Singlet States. *J. Mol. Struct.* **2022**, *1252*, 132053.

(42) Oeltermann, O.; Brand, C.; Wilke, M.; Schmitt, M. Ground and Electronically Excited Singlet State Structures of the Syn and Anti Rotamers of 5-Hydroxyindole. *J. Phys. Chem. A* **2012**, *116*, 7873–7879.

(43) Wilke, M.; Brand, C.; Wilke, J.; Schmitt, M. Influence of the Position of the Methoxy Group on the Stabilities of the Syn and Anti Conformers of 4-, 5-, and 6-Methoxyindole. *J. Mol. Spectrosc.* **2017**, *337*, 137–144.

(44) Brand, C.; Oeltermann, O.; Pratt, D.; Weinkauf, R.; Meerts, W. L.; van der Zande, W.; Kleinermanns, K.; Schmitt, M. Rotationally Resolved Electronic Spectroscopy of 5-Methoxyindole. *J. Chem. Phys.* **2010**, *133*, 024303.

(45) Brand, C.; Oeltermann, O.; Wilke, M.; Schmitt, M. Position Matters: High Resolution Spectroscopy of 6-Methoxyindole. *J. Chem. Phys.* **2013**, *138*, 024321.

(46) Fleisher, A. J.; Morgan, P. J.; Pratt, D. W. Charge Transfer by Electronic Excitation: Direct Measurement by High Resolution Spectroscopy in the Gas Phase. *J. Chem. Phys.* **2009**, *131*, 211101.

(47) Fleisher, A. J.; Young, J. W.; Pratt, D. W.; Cembran, A.; Gao, J. Flickering Dipoles in the Gas Phase: Structures, Internal Dynamics, and Dipole Moments of β-Naphthol-H_2O in Its Ground and Excited Electronic States. *J. Chem. Phys.* **2011**, *134*, 114304.

(48) Borst, D. R.; Korter, T. M.; Pratt, D. W. On the Additivity of Bond Dipole Moments. Stark Effect Studies of the Rotationally Resolved Electronic Spectra of Aniline, Benzonitrile, and Aminobenzonitrile. *Chem. Phys. Lett.* **2001**, *350*, 485–490.

(49) Larsen, N. W. Microwave Spectra of the Six Mono-^{13}C-Substituted Phenols and of Some Monodeuterated Species of Phenol. Complete Substitution Structure and Absolute Dipole Moment. *J. Mol. Struct.* **1979**, *51*, 175–190.

(50) Reese, J. A.; Nguyen, T. V.; Korter, T. M.; Pratt, D. W. Charge Redistribution on Electronic Excitation. Dipole Moments of Cis- and Trans-3-Aminophenol in Their S_0 and S_1 Electronic States. *J. Am. Chem. Soc.* **2004**, *126*, 11387–11392.

(51) Schneider, M.; Wilke, M.; Hebestreit, M. L.; Henrichs, C.; Meerts, W. L.; Schmitt, M.

Excited-State Dipole Moments and Transition Dipole Orientations of Rotamers of 1,2-, 1,3-, and 1,4-Dimethoxybenzene. *ChemPhysChem* **2018**, *19*, 307–318.

(52) Bofill, J. M.; Quapp, W.; Albareda, G.; Moreira, I. de P. R.; Ribas-Ariño, J. Controlling Chemical Reactivity with Optimally Oriented Electric Fields: A Generalization of the Newton Trajectory Method. *J. Chem. Theory Comput.* **2022**, *18*, 935–952.

(53) Bunker, I.; Ayinla, R. T.; Wang, K. Single-Molecule Chemical Reactions Unveiled in Molecular Junctions. *Processes* **2022**, *10*, 2574.

(54) Gorenskaia, E.; Turner, K. L.; Martín, S.; Cea, P.; Low, P. J. Fabrication of Metallic and Non-Metallic Top Electrodes for Large-Area Molecular Junctions. *Nanoscale* **2021**, *13*, 9055–9074.

(55) Escorihuela, E.; Concellón, A.; Marín, I.; Kumar, V. J.; Herrer, L.; Moggach, S. A.; Vezzoli, A.; Nichols, R. J.; Low, P. J.; Cea, P. et al. Building Large-Scale Unimolecular Scaffolding for Electronic Devices. *Mater. Today Chem.* **2022**, *26*, 101067.

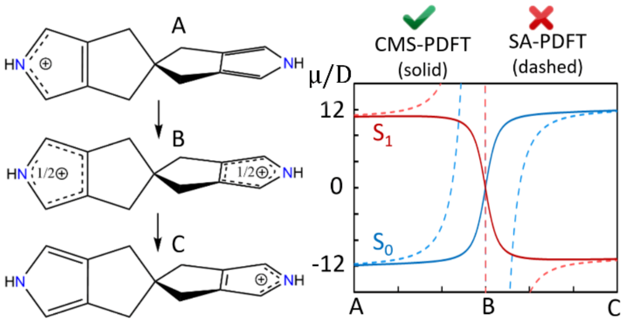

TOC Graphic